Characterization of corrosion in reinforced concrete beams using destructive and non-destructive tests

Tomasz Ferenc [*], Erwin Wojtczak, Błażej Meronk, Magdalena Rucka

Gdansk University of Technology, Faculty of Civil and Environmental Engineering, Poland

A R T I C L E   I N F O

A B S T R A C T

The paper presents both non-destructive and destructive experimental tests on steel-reinforced concrete beams subjected to electrochemical corrosion. To examine the condition and behavior of the specimens, destructive tests were carried out, i.e., a three-point bending together with a modulated ultrasonic wave test. In addition, a series of non-destructive experiments were conducted, such as the potential measurement method, low-frequency vibrations, and ultrasonic wave propagation. A three-point bending test was conducted to examine the behavior of specimens under applied quasi-static force, together with a modulated ultrasonic wave test. The force-displacement relation, capacity, failure displacement, flexural stiffness, and failure mode were determined for each specimen. A modulated ultrasonic wave test was also performed during the flexural test. Prior to this, the specimens were visually inspected to check if any cracks occurred and a series of non-destructive tests such as potential measurement, low-frequency vibrations, and ultrasonic wave propagation were then performed.

1. Introduction

Cement-based materials, such as concrete reinforced with steel bars, are one of the most commonly used materials in civil and industrial structures. Their high mechanical properties, high strength, relatively low cost, durability, ease of production and maintenance, and ability to be formed into various shapes, as well as their non-combustibility, high-temperature resistance, and low porosity make them widely used throughout the world [1]. Although they have many of the advantages listed above, they also show some disadvantages. On the one hand, reinforced concrete (RC) can withstand many loads, such as static and dynamic loads, e.g., earthquakes, strong winds, or aggressive environments, e.g., seawater, sewage, or chemical reagents. On the other hand, over time, all these factors can eventually break down the structures and cause them to collapse. The critical factors are, generally, overload, dynamic loading, and related fatigue, as well as environmental conditions in which structures are exploited [2–8].

Steel-reinforced concrete structures are highly susceptible to corrosion, which is one of the main causes of structural damage and its early collapse [9]. Corrosion causes the deterioration of the steel reinforcement, which is usually placed in the concrete in the form of bars. The corrosion process leads to a reduction in the cross-section area of the reinforcement, thereby reducing the load-bearing capacity of the structure. Moreover, it leads to the formation of expanded corrosion products, which can cause cracking in the concrete and spalling of the concrete cover [10–13]. This, in turn, causes the loss of the protective layer of concrete that protects the steel reinforcement from an aggressive environment. The thickness of the cover is usually assumed according to standards, e.g., EN 1992

Eurocode 2: Design of concrete structures, and depends on a few factors, e.g., on the environmental conditions in which structures are exploited or steel reinforcement diameter. Incorrect design of the cover can be a starting point for the corrosion process and may lead to catastrophic failure of the whole structure. Furthermore, the steel reinforcement inside the concrete is protected by a thin, passive film of hydrated iron and calcium oxides (Fig. 1) [14]. However, external factors such as carbon dioxide (CO_2) or other aggressive substances such as chlorides from salt water can damage the passive layer, resulting in a potential difference. This can be a starting point for corrosion which is generally considered to be an electrochemical process. The process causes the formation of rust, i.e. iron oxides, at anodic sites, along with the release of electrons. The electrons are then conducted through the steel bar to cathodic sites, where they undergo oxygen depolarization with the formation of hydroxide ions (OH-) [15].

Corrosion usually occurs without significant external symptoms as the reinforcing bars are embedded in the concrete and it is impossible to visually assess their actual condition state. Hence, it is crucial for the safety of structures to use integrated non-destructive or destructive diagnostic techniques to detect and evaluate corrosion at different stages [16].

To perform laboratory tests that allow the assessment of the condition state of reinforced concrete specimens without or with different levels of corrosion, the corrosion process must be artificially induced. Accelerated electrochemical corrosion is usually initiated to reduce the time for the process to take place. Specimens are immersed in the corrosive electrolyte, such as sodium chloride (NaCl) solution with a concentration of approximately 3–3.5 % [17,18]. To accelerate the process, the specimens are connected to a power supply that generates constant current flowing through. To create a closed circuit, the specimen reinforcement is connected to the positive pole and constitutes the anode, while the other steel rod is freely immersed in the solution and is connected to the negative pole and acts as the cathode. A current of constant density is usually assumed with a value corresponding to 0.2–0.3 mA/cm^2 [18–22].

Specimens subjected to corrosion may be examined using both non-destructive and destructive methods. However, non-destructive methods become more crucial hence the corrosion is often invisible during visual inspection. One of the main methods is to measure the potential difference between the reinforcement of the RC element and a reference electrode placed on its outer surface [23–26]. Moreover, papers [19,21,27] present an approach in which natural frequencies and mode shapes are determined and their variation as the corrosion process progresses is studied. In addition, methods based on guided waves penetrating RC elements and variations of their velocities are given in [20,28,29]. X-ray computed tomography is also used to monitor the occurrence of corrosion in RC [30–32]. In addition, acoustic emission (AE) is an effective method for evaluating and real-time ongoing monitoring of corrosion occurrence and degradation in RC caused by it [33–35].

Given the above aspects of the research carried out to date, it is essential that further research is carried out using combined methods, both non-destructive and destructive, to investigate the effect of corrosion on the behaviour of RC structures in a more complex approach. In this paper, both non-destructive and destructive experimental tests were carried out on steel-reinforced concrete beams with different levels of corrosion. To investigate the condition state and behavior of the specimens, destructive tests were carried out, such as a three-point bending test to verify the force-displacement relation, capacity, and failure mode of the specimens together with a modulated ultrasonic wave test. This was preceded by a series of non-destructive experiments, such as potential measurement method, low-frequency vibrations, and ultrasonic wave propagation.

2. Description of specimens

2.1. Materials

A total number of ten reinforced concrete beams, designated C0-C9 (C-series beams), were analyzed in the paper. The specimens were prepared in the same way, in a single manufacturing process using concrete, water, cement, aggregate, and admixture keeping a ratio W/C equal to 0.5. The Portland cement type CEM I 42.5 R was used. The fine aggregate was naturally washed sand with a grain size of 0–2 mm and the coarse aggregate was natural pebbles with a grain size of 2–8 mm and 8–16 mm, both with densities equal to 2.65 kg/dm^3. The superplasticizer was also added to improve the homogeneity and workability of the concrete mix. The exact recipe for the concrete is presented in Table 1. A mechanical mixer was used to mix all the components. After the concrete cured for 28 days, the compressive strength was determined on five cubic specimens with dimensions of $150 \times 150 \times 150$ mm^3. The mean value was 39.27 MPa.

A single steel bar with a diameter of ϕ10 mm and a length of 930 mm was used as a reinforcement. The bar is made of a B500SP steel class with a yield point equal to f_{yk} = 500 MPa. The chemical composition of the steel is summarized in Table 2. The carbon equivalent (C_{eq}) does not exceed $C_{eq,max}$ = 0.52 %.
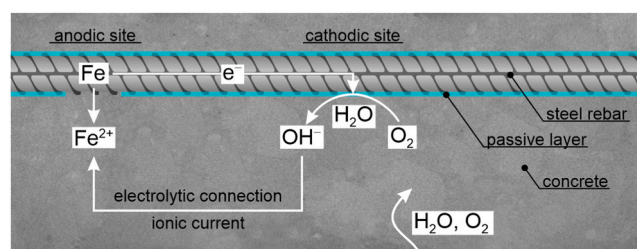

Fig. 1. The scheme of the corrosion process (redrawn after [15]).

Table 1
The recipe for concrete.

No	Component	Amount
1	cement CEM I 42.5 R	330 kg/m^3
2	water	165 kg/m^3
3	aggregate (sand) 0–2 mm	710 kg/m^3
4	aggregate (gravel) 2–8 mm	664 kg/m^3
5	aggregate (gravel) 8–16 mm	500 kg/m^3
6	superplasticizer	2.31 kg/m^3

2.2. Specimens

All the specimens tested had dimensions of $100\times150\times1000$ mm^3 (Fig. 2a). A single steel reinforcing bar was placed inside each sample, in the center of the width of the cross-section and with a bar cover equal to 35 mm from the bottom surface of the specimen (Fig. 2b). The bars were specially prepared before being placed in position and the concrete mixture was poured into the formwork. To initiate the corrosion process in the samples, the end of each bar was connected to a 1 mm wire and then was secured with heat shrink tubing.

Nine specimens (C1-C9) were subjected to the corrosion process and then examined, while the tenth (C0) was a reference one, which did not undergo corrosion.

3. Description of methods

The following measurements of specimen properties, both destructive and non-destructive ones, were conducted after the corrosion in the samples was induced. Destructive tests were performed together with non-destructive ones. Three-point bending tests were carried out to determine the stiffness of the specimen and its capacity with failure mode under bending, together with a modulated ultrasonic wave test. Both tests were conducted in parallel in order to find if any relationship between obtained results may be observed, e.g. if non-destructive tests could predict damage on the analyzed beams before its occurrence.

Additionally, before destructive tests, non-destructive methods, such as electrical potential measurement, low-frequency vibrations, and ultrasonic waves were used. Moreover, the influence of corrosion on beam mechanical parameters was investigated.

3.1. Accelerated electrochemical corrosion

Electrochemical corrosion was induced in concrete beams C1-C9 by immersing the samples in a 3.5 % sodium chloride (NaCl) solution for several days. To accelerate the corrosion process, the steel reinforcing bar and the additional bar, also placed in the solution, were connected to a laboratory power supply as an anode and cathode, respectively (Fig. 3). This connection allowed a constant current to be generated and passed through the specimen. The value of the current density was assumed to be 90 mA, which corresponds to 0.3 mA/cm^2 taking into account the total surface area of the rebar.

To investigate the effect of corrosion on the behavior and material parameters of reinforced concrete beams, nine specimens were immersed for a predetermined number of days – from 1 to 35. The specimen designated as C1 was immersed for the shortest period, i.e. for 1 day, while the remaining specimens (C2-C9) were immersed for a longer time so that specimen C9 was immersed for a period equal to 35 days. The exact number of days the specimens were kept in solution is given in Table 3.

3.2. Three-point bending test

To investigate static behavior such as stiffness, capacity, and failure modes of each specimen with different levels of corrosion (C0-C9), three-point bending tests were conducted. The test stand is presented in Fig. 4. As the length of the specimen was 1000 mm, the span length during the experiments was equal to 900 mm with a single force applied at the centre. Both the cross-head and the support were made of steel and had the shape of half-cylinders with a radius of 40 mm. The tests were carried out on a Zwick/Roell Z400 testing machine with a capacity of 400 kN. The speed of the cross-head was 1 mm/min. During experiments applied force (P) and cross-head path (u) were recorded. The tests were performed until the specimens failed.

Before the tests were conducted, the capacity of the reference specimen C0, thus not exposed to corrosion, was calculated. The maximum force that can be applied to the specimens was calculated using equations based on the European standards for reinforced concrete design, i.e., Eurocode 2 (EC2). The maximum internal bending moment (cross-section bending capacity) was determined from the equation, for rectangular cross-section, individually reinforced:

Table 2
The chemical composition of the steel.

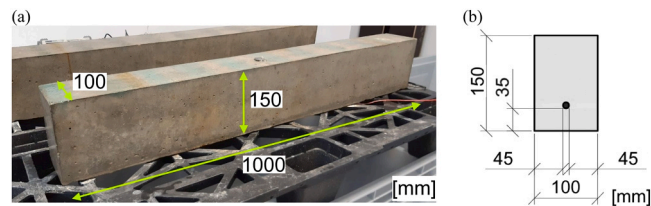| C	Mn	Si	P	S	Cu	N
0.25 %	1.65 %	0.60 %	0.055 %	0.055 %	0.85 %	0.013 %

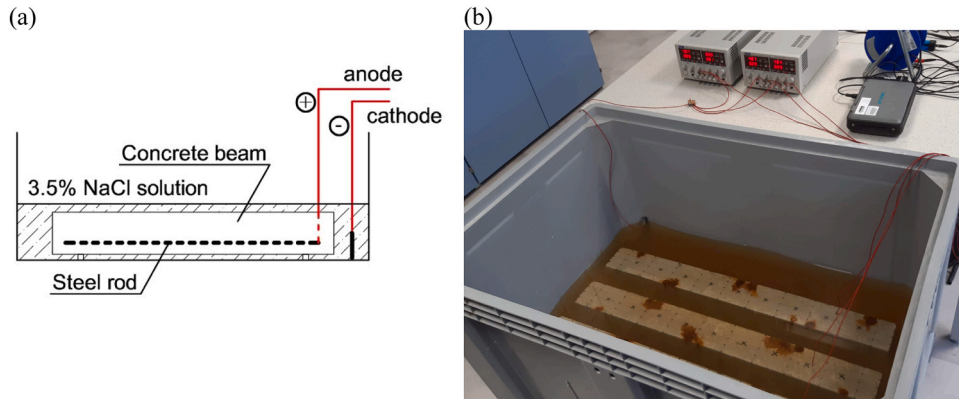**Fig. 2.** Beam specimen: (a) overall view, (b) cross-section.

Fig. 3. Experiment setup of accelerated electrochemical corrosion: (a) scheme, (b) overall view.

$$M_{Rd} = \xi_{eff}bd^2f_{cd}(1 - 0.5\xi_{eff}) = 3.49 kNm. \tag{1}$$

Based on the moment, the external force that damage the specimen was estimated at $P_{max} = 15.48$ kN.

3.3. Modulated ultrasonic wave test

Studies were carried out using a modulated ultrasonic wave during a three-point bending test. The positioning of the transducers was selected in such a way that the ultrasonic wave propagated along the sample (see Fig. 4). A wave emitter was placed at one end of the beam. Ultrasonic wave-receiving sensors were placed on the bottom of the beam at points a2 and a8 (see Fig. 6). A continuous wave with a frequency of 58 kHz amplitude modulated with a 1 kHz frequency signal was used. The modulation depth was set to 100 %. The signal was generated by an arbitrary function generator using the DDS method. The signal was recorded with a sampling frequency of 2 MHz. The length of each recorded signal was 0.25 seconds. The signal was recorded at two points simultaneously. Measurements were taken for all specimens before the start of the destructive bending test and after each load increase of 1 kN, until the element was destroyed. The proposed measurement method is based on the analysis of the frequency spectrum of the recorded signal. In the case of a sample of the material with a material structure allowing linearly elastic wave propagation, the expected spectrum of the signal is the same as the wave generated by the transmitter and should consist of three distinct components: a carrier wave with a frequency of 58 kHz and two additional components with a half-lower amplitude at sideband frequencies of 58 kHz ± 1 kHz resulting from amplitude modulation of the signal. These additional components should have an amplitude equal to half the amplitude of the carrier wave. If areas with strongly nonlinear elastic properties appear in the specimen, the ultrasonic wave is deformed and its frequency spectrum changes its character.

3.4. Corrosion potential measurement

Corrosion potential measurements were performed to assess the occurrence of corrosion in steel-reinforced concrete beams. The method used in the paper is described in ASTM C876–15 standard and is based on the measurement of the potential difference between the corroded steel rod and a reference electrode placed on the concrete surface (Fig. 5). A high-impedance voltmeter manufactured by Proceq (Profometer Corrosion) was used together with reference electrode with the copper–copper (II) sulfate (Cu|CuSO4) (E0 = 0.314 V vs SHE).

Based on the measured values of potential difference between the steel rod and the reference electrode placed on the surface of the concrete specimens, the possibility of corrosion occurrence can be assessed. The aforementioned ASTM standard provides three ranges of measured potential: if the potential is –350 mV or lower then the probability of corrosion is 90 %, if the potential is –200 mV or higher then the probability of corrosion is lower and equal to 10 %, and if the measured potential is between these values – the result is uncertain. In general, values of potential vary between –1000 mV and +200 mV, and as the potential decreases, the probability of
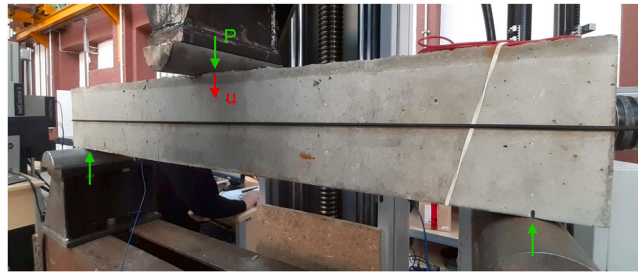
Table 3
Measurement designation and the corresponding number of days that specimens spend in the solution.

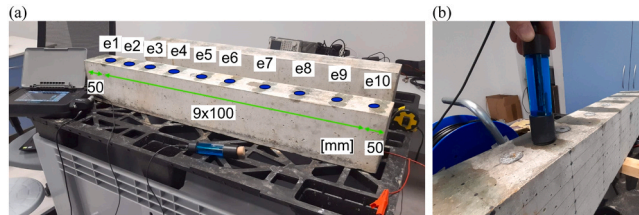| beam	days	1–10										11–20										21–30										31–35				
C0	0																																			
C1	1	x																																		
C2	2	x	x																																	
C3	3	x	x	x																																
C4	5	x	x	x	x	x																														
C5	7	x	x	x	x	x	x	x																												
C6	14	x	x	x	x	x	x	x	x	x	x	x	x	x	x																					
C7	21	x	x	x	x	x	x	x	x	x	x	x	x	x	x	x	x	x	x	x	x	x														
C8	28	x	x	x	x	x	x	x	x	x	x	x	x	x	x	x	x	x	x	x	x	x	x	x	x	x	x	x	x							
C9	35	x	x	x	x	x	x	x	x	x	x	x	x	x	x	x	x	x	x	x	x	x	x	x	x	x	x	x	x	x	x	x	x	x	x	x

Fig. 4. Bending test set-up.

Fig. 5. Experiment setup for corrosion potential measurement.
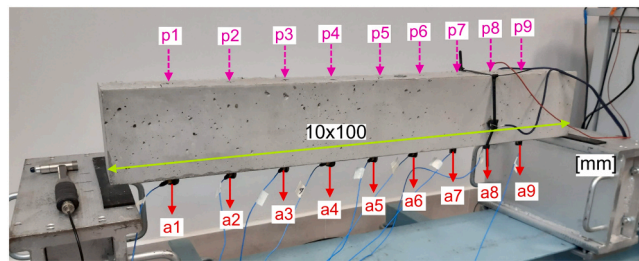

Fig. 6. Location of accelerometers (a1-a9) and applied impulse forces (p1-p9) for low-frequency vibrations.

corrosion increases.

A reference electrode was used to measure the potential which was placed at ten points along the concrete beams with an interval of 100 mm and three points across the width. In this way, the potential difference between the steel rod and the reference electrode was measured at thirty points. However, as the measured values were usually similar across the width of the specimens, they were averaged and the results were finally presented in ten points (e1-e10) arranged along the length of the specimens.

3.5. Low-frequency vibrations

The specimens were freely placed in steel supports spaced 950 mm apart to measure their free vibrations and determine their natural frequencies and mode shapes. A modal hammer (PCB Piezotronics Inc) was applied to produce impulse loading and inducing vibrations. Both, the applied force $p_k(t)$ and the structural response in the form of acceleration $a_i(t)$ were measured at nine points p1-p9 and a1-a9, respectively (Fig. 6). The measured signals were collected using the Siemens PLM Software LMS SCADAS acquisition system.

The measured values $a_i(t)$ and $p_k(t)$ were transformed by the Fast Fourier Transform (FFT) into frequency-dependent signals $a_i(\omega)$ and $p_k(\omega)$. Then Frequency Response Functions (FRFs) were calculated from the formula

$$H_{ik}(\omega) = \frac{a_i(\omega)}{p_k(\omega)},$$

(2)

where $H_{ik}(\omega) = \mathbf{H}(\omega)$ is FRF in the form of a matrix with i rows and k columns. On this basis, natural frequencies and mode shapes were determined. Moreover, FRFs can also lead to the determination of damping ratios, however, this was not done in the paper.

Each element of the matrix $\mathbf{H}$ can be represented graphically. As an example, Fig. 7a shows the element $abs(H_{4,5}(\omega))$ which is the absolute value of the FRF obtained as the quotient of the measured signals: the impulse load applied at point p5 and the structural response (acceleration) measured at point a4, both in the frequency domain. The values of the natural frequencies were read from the

abscissae where the peaks of the $abs(H_{ik}(\omega))$ function occur. In the considered range of frequency, from 0 to 2700 Hz, three natural frequencies were observed. To improve accuracy, all values around the first, second, and third frequencies were read and then averaged. Furthermore, the FRFs were smoothed and approximated according to the Gauss function to further improve accuracy.

To obtain the mode shapes of the free vibrations, the imaginary part of the FRFs $imag(H_{ik})$ was calculated. Then, a single row or column of the matrix has to be selected, e.g., the fifth row consists of the measured signals at point a5 induced by the impulse load applied at points p1-p9. Next, to determine each mode shape, every element from the selected row amplitudes of $imag(H_{ik})$ must be identified in each element of the selected row, taking into account both its value and the location of the points along the length of the specimen. This can lead to a graphical form of mode shapes. The example of the third mode shapes is presented in Fig. 7b.

3.6. Ultrasonic waves

Additional tests were performed with the use of an ultrasonic pulse velocity analyzer (UPV). The experimental set-up (Fig. 8a) consisted of a Pundit PL-200 Technique unit (Proceq) and two exponential P-wave transducers with a carrier frequency of 54 kHz. According to the manufacturer's recommendations, the transducers can be used if the maximum grain size does not exceed 34 mm and the minimum dimension of the tested sample is not less than 69 mm; both these requirements are satisfied in the current study. The transducers do not require using gel couplant, providing fast and robust measurements. The transducers utilize the through-transmission measuring approach. During measurements, one of the transducers acts as an exciter, generating an electric signal in the form of a sinusoidal wave packet, while the second acts as s sensor, receiving the signal after propagation through the sample. The device estimates the time of flight (TOF) of the wave based on the appearance of the first wave packet in the recorded signal. The signal can also be stored for further analysis.

The propagating P-wave signals for both measurements were collected in several paths numbered 1–156 (Fig. 9), running from side to side of each beam (paths 1–96) and from the top to bottom (paths 97–156). A 3D printed stencil was prepared to ensure accurate positioning of the measurement points on the surface of the beams and to minimize the time required for the investigations. The measurements were taken three times in each path to verify the repeatability of the signals and to provide more accurate results. The collected data were further processed using Matlab® software to determine the time of flight (TOF) of the wave. As a result, the P-wave velocity was calculated for each path based on the TOF and the lengths of the wave propagation paths. An example of a signal containing the results is presented in Fig. 8b.

4. Results and discussion

4.1. General observations

As mentioned above, specimens C1-C9 were immersed in a 3.5 % NaCl solution for the specific number of days specified in Table 3 to induce corrosion. As the process progressed, cracks were expected to appear in the specimens. Hence, after removal from the solution, their surfaces were carefully examined for the cracks appearance.

Samples C1 and C2, which were kept in the solution for the shortest time, i.e. 1 and 2 days respectively, showed no cracking or other surface changes. However, cracks were observed in other specimens (C3 to C9) that were immersed for a longer period, i.e. from 3 to 35 days. The location of the cracks was schematically presented in Fig. 10, on five views of each sample: the bottom view is given in the middle, the two side views are shown above and below, and the front views are given on the left and the right. It can be observed, is cracks first appeared at the bottom surface of the specimens, along the reinforced steel rods (see C3, C4, and C5). This may be due to the fact that the distance from the rebar to the bottom surface is the smallest (the thinnest layer of concrete covers the bar). Then, cracks appeared on the front surfaces and side surfaces as well. Generally, the longer the specimens were kept in the solution, the more cracks occurred.

Finally, the selected specimens were cut into approximately 100 mm thick slices to observe the occurrence of internal corrosion (Fig. 11). Generally, corrosion appeared locally, on the surface of the reinforced steel bar. From this area, the cracks spread radially and randomly, leaving out the aggregates.
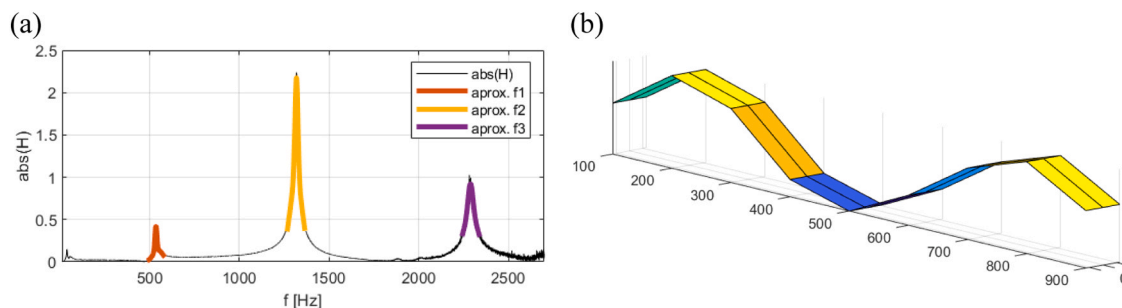

Fig. 7. (a) absolute value of chosen frequency response function FRF - $abs(H_{4,5}(\omega))$, (b) the third mode shape.
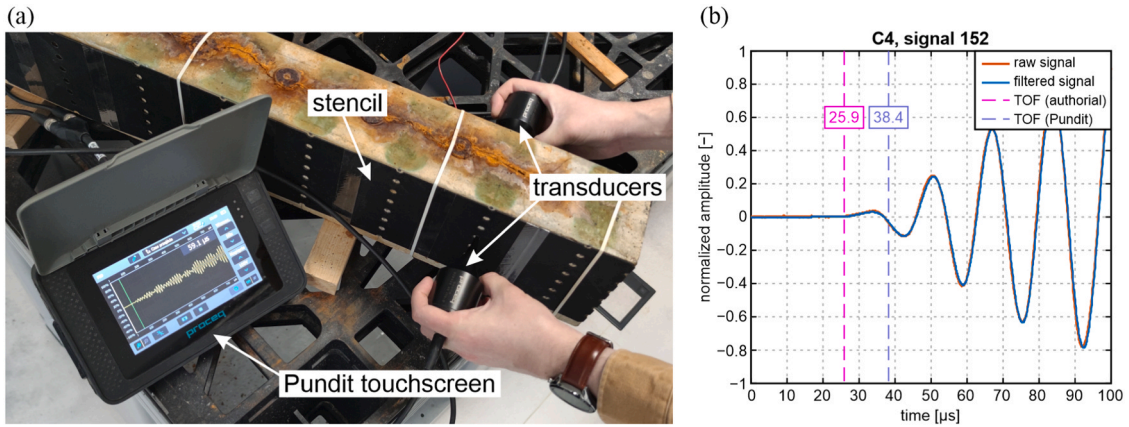
(a)

(b)

Fig. 8. (a) Experiment set-up, (b) The example of signals measured while experiments with a self-written algorithm.
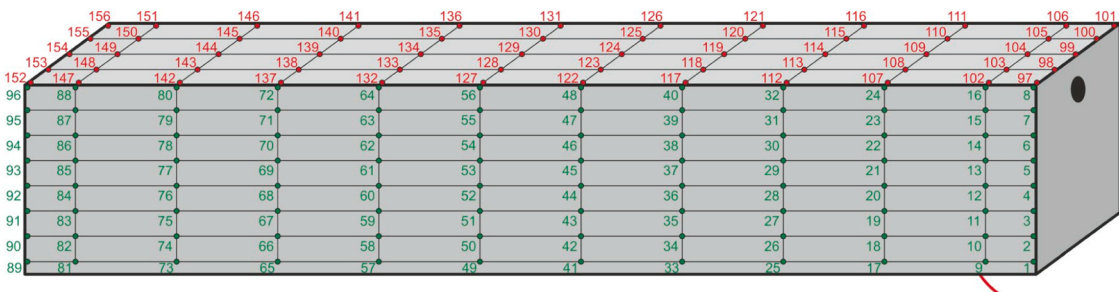

Fig. 9. Scheme of measurement points in tests with UPV.

4.2. Three-point bending tests

As mentioned earlier, the three-point bending tests were carried out to determine beam stiffness (force-displacement curve), beam capacity, and failure modes.

First, the relationships between applied force and displacement at the centre of specimen length were presented graphically in Fig. 12.

During experiments, the first cracks started to appear in the middle of the length of the specimen, in the bottom areas of the cross-section. Two types of failure modes can be distinguished for different specimens. The first one, designated as "type A", is typical for concrete structures reinforced with a single bar known as a flexural failure. In this mode, the cracks propagated together with the increase of their width. From a certain point, only a single steel bar carried the internal bending moment caused by the applied force until the stress level reached its yield point. The second failure mode, designated as "type B" also known as a shear failure, was characterized by cracks appearing at an angle of about 45° or less. This means that it was not the bending moment but the shear force that determined the achievement of the load capacity. While the level of the applied load increased, the width of cracks increased, until the specimens failed, which occurred when the steel rod lost adhesion to the concrete and detached. The specimens subjected to corrosion for more days showed type B of failure mode (shear failure), i.e., specimens C6-C9 (Table 4). This proves that the presence of corrosion weakens the bond between the concrete and steel reinforcement. The examples of both types of failure modes are presented in Fig. 13. Moreover, Fig. 14 shows the specimen after destruction according to type B, where the rebar detached from the concrete.

Additionally, Table 4 includes the values of maximum applied force, maximum displacement, and flexural stiffness determined in the range of displacement from 1 to 2 mm. The lowest value of the force was applied to specimens C7-C9, which were immersed in NaCl solution for the longest number of days, i.e. 19.6 kN, 20.81 kN, and 17.36 kN, respectively. In general, the shorter the time the specimens were subjected to corrosion, the higher the load carrying capacity. However, the highest capacities of 23.59 kN and 23.1 kN were obtained for specimens C3 and C4, respectively, whereas the capacities for specimens C1 and C2 were 22.71 kN and 20.97 kN, respectively. The highest failure displacements were measured for specimens C5 and C8 and they were 5.59 mm and 5.11, respectively. On the other hand, the lowest displacement was measured for the not corroded specimen C0, which was equal to 3.42 mm. In terms of flexural stiffness, the longer the corrosion time, the lower the flexural stiffness. The values ranged from 142.90 kNm^2 for specimen C0 to 69.66 kNm^2 for specimen C9.
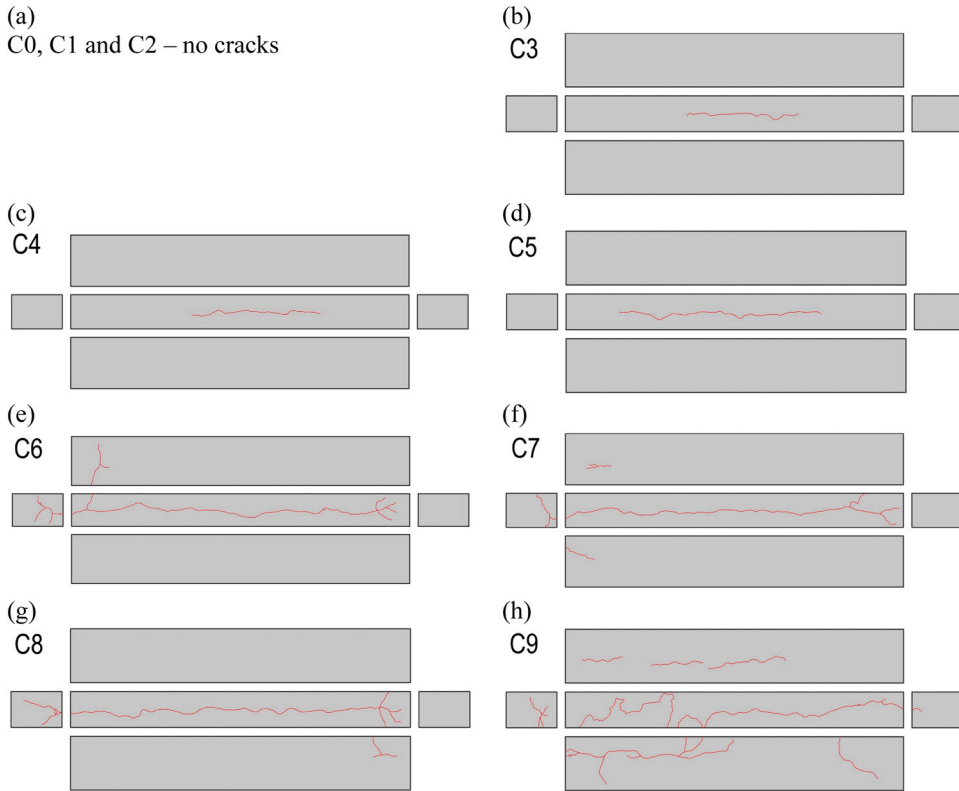
(a)
C0, C1 and C2 – no cracks

(b)
C3

(c)
C4

(d)
C5

(e)
C6

(f)
C7

(g)
C8

(h)
C9

Fig. 10. Observed cracks for different specimens C0-C9 after immersion in NaCl solution.
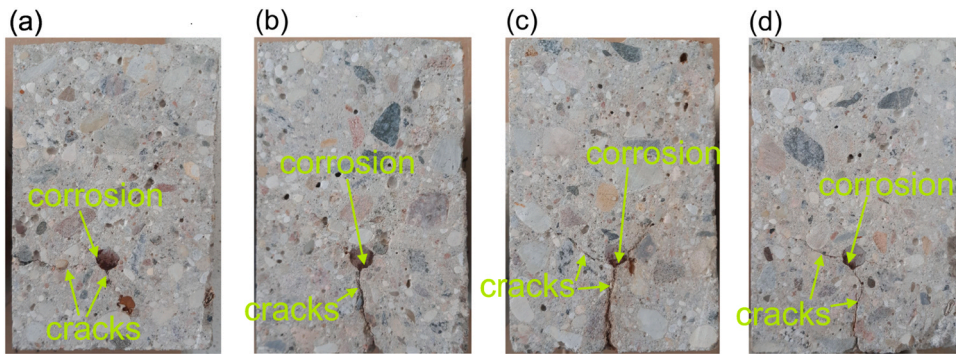
(a)   (b)   (c)   (d)

Fig. 11. The corrosion and cracks occurrence inside the specimen.

4.3. Modulated ultrasonic wave test

A frequency analysis of the recorded signals was carried out. For measurements prior to the destructive test, all spectra of the ultrasonic signals looked similar as shown in Fig. 15. The spectra consisted of a dominant component with a frequency of 58 kHz and one component with a frequency of 57 kHz and 59 kHz. The amplitudes of the side band components were usually smaller than the amplitude of the carrier wave (Fig. 15a). However, at some levels of the applied force, the sideband components were higher than the middle one (Fig. 15b), which may indicate the occurrence of new of cracks.

The results for each specimen, including the level of applied force, are presented in Fig. 16, where the lines represent the spectra consisting of components with different frequencies. The black line represents the dominant frequency of 58 kHz, while the green and blue lines represent sideband frequencies of 57 kHz and 59 kHz, respectively. The amplitudes of spectra were normalized so that the dominant component was always 1, and the sideband components were usually lower. However, for some levels of applied force, the sideband components were higher.

For example, for specimen C9, no significant difference was observed between the specimens in the pre-load state (see Fig. 16i).
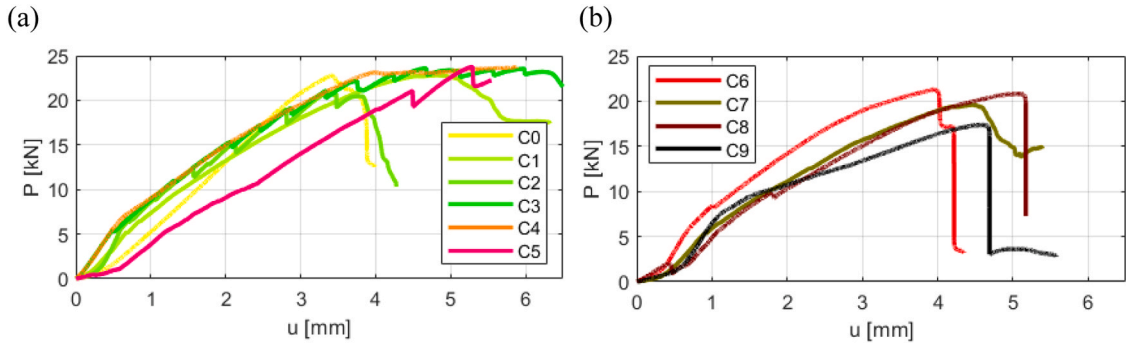
Fig. 12. Force-displacement function while three-point bending tests for specimens: (a) C0-C5, (b) C6-C9.

Table 4
Summarized results for three-point bending test.

Specimen	C0	C1	C2	C3	C4	C5	C6	C7	C8	C9
Type of failure mode	A	A	A	A	A	A	B	B	B	B
Maximum applied load [kN]	22.78	22.71	20.97	23.59	23.1	22.35	21.29	19.6	20.81	17.36
Failure displacement [mm]	3.42	4.54	3.36	4.67	4.54	5.29	3.96	4.47	5.11	4.63
Flexural stiffness [kNm^2]	142.90	105.39	103.60	102.71	101.90	92.88	110.74	94.67	100.03	69.66

Fig. 13. Two types of failure modes: (a) type A – flexural failure, (b) type B – shear failure.

Fig. 14. Specimen after destruction with type B.

With a gradual increase in the force applied to the specimens, insignificant changes in the signal spectrum were observed until the appearance of cracks. In the initial phase, when the cracks were barely visible, characteristic spectra were recorded, where the amplitude values in the sidebands were higher than the amplitude of the carrier wave. After opening the cracks, the spectra of the signal returned to a form similar to that in the initial phase.

Generally, for samples that exhibited a type B mode (shear failure), this phenomenon was observed once, and for samples that were destroyed according to a type A mode (flexural failure), the phenomenon occurred twice during the increase in load, except for specimens C1 and C5. The values of the measured load at which the amplitude values occurred in the sidebands were higher than the amplitude of the carrier wave are shown in Table 5.
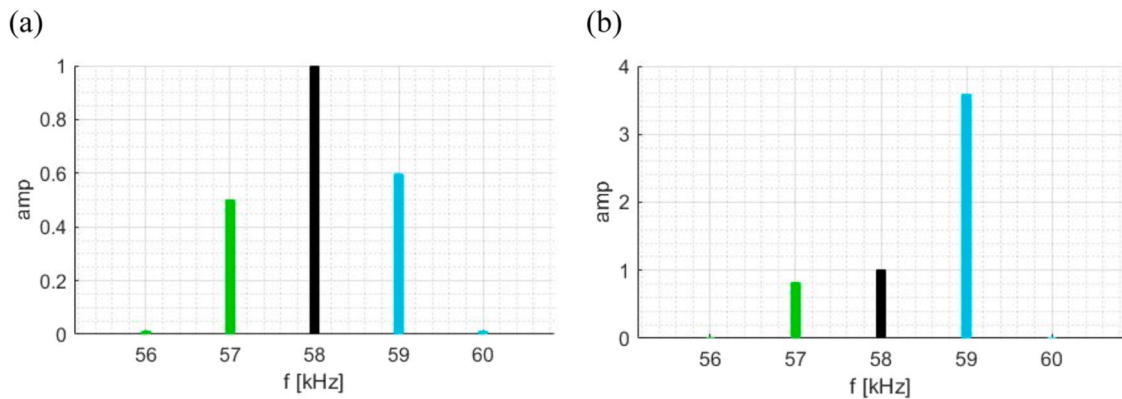
Fig. 15. Spectra of ultrasonic signals measured for specimen C9 for applied force: (a) 5 kN, (b) 10 kN.

Moreover, the deformation of the spectrum was much greater at point a2, located further from the inductor than a8 located close to the wave source. The cracking zone was located between points a2 and a8.

4.4. Corrosion potential measurement

Corrosion potential measurements were conducted after the specimens were subjected to corrosion for the time mentioned above. The specimens were removed from the NaCl solution and left to dry for approximately 18 h. The potential difference that occurred between the reference electrode placed on the bottom surface of the specimens and the reinforced steel bar was then measured. The results for all specimens are presented graphically in Fig. 17. The values of potential are given on the vertical axis, while the horizontal axes show: the number of days that each specimen was immersed in the solution and the localization of measuring points e1-e10. Additionally, labels with sample designations were added to the graph.

The values of the measured potential difference between a reference electrode and a steel bar varied from about –440 mV for specimens that were immersed in NaCl solution for the shortest time (C1 and C2), to about –740 mV (both vs Cu|CuSO$_4$). The mean values of the measured potential are listed in Table 6.

The highest measured potential was obtained for specimens C9 and C8. The specimens were kept in NaCl solution for one and two days, respectively. Moreover, no cracks were observed after they were removed from the solution. Then, a significant drop in the values of measured potential can be noticed. The values of measured potential decreased by about 35 % in specimen C3 compared to C2. Such a significant difference in potential may be caused by the occurrence of the first cracks in specimen C3 (see Fig. 10b). The values of the potential in the following specimens continue to decrease, but much slower – for about 9 % between specimen C4 compared to C3, and for about 3 % between C5 compared to C4. However, from specimen C5, the values of the measured potential started to increase slightly (for about 4 % between C6 compared to C5) and then remained at a similar level with a variation of less than 3 % between.

It is worth noting that the distribution of the measured potential between the reference electrode and the reinforced steel bar along the length of each specimen was fairly uniform. Only a slight difference in measured potential can be observed at points e1-e10.

4.5. Low-frequency vibrations

Each specimen was examined to determine its natural frequencies and mode shapes before and after immersion in the NaCl solution. The obtained values are listed in Table 7, which consists of the values determined for the first, the second, and the third natural frequencies.

The first, second, and third natural frequencies before immersion in the solution for all specimens ranged from 496 Hz to 535 Hz, from 1237 Hz to 1315 Hz, and from 2155 Hz to 2293 Hz, respectively. After immersing the specimens for a predetermined number of days, all frequencies increased (see Table 7). However, to make the values of the increases comparable, the values of all three frequencies before immersion were reduced to 100. The value of the increase was then calculated and plotted in Fig. 18a-c.

The highest increase of all three frequencies was obtained for specimen C1 which was kept in the solution for 1 day. This increase was approximately 7.5 %, 6.8 %, and 6.2 % for the first, the second, and the third frequencies, respectively. This may be due to the samples absorbing water after being placed in the solution. However, the next specimen C2 showed a smaller increase, i.e. approximately 4.4 % for f_1, 4.3 % for f_2, and 3.7 % for f_3. Then, for the following specimens (C3 to C5) the increase appeared to be about 6.8 % for f_1, 6.7 % for f_2, and 6.0 % for f_3. After that point, i.e., for specimens C6-C7, the increase remained at the same level (about 7 % for f_1, about 6.4 % for f_2, and 5.9 % for f_3), while for specimens C8-C9 the increase was lower – from 5.9 % to 3.6 %.

4.6. Ultrasonic waves

The values of P-wave velocity were presented in the form of maps drawn individually for each beam for both measurements

(a) C1

(b) C2

(c) C3

(d) C4

(e) C5

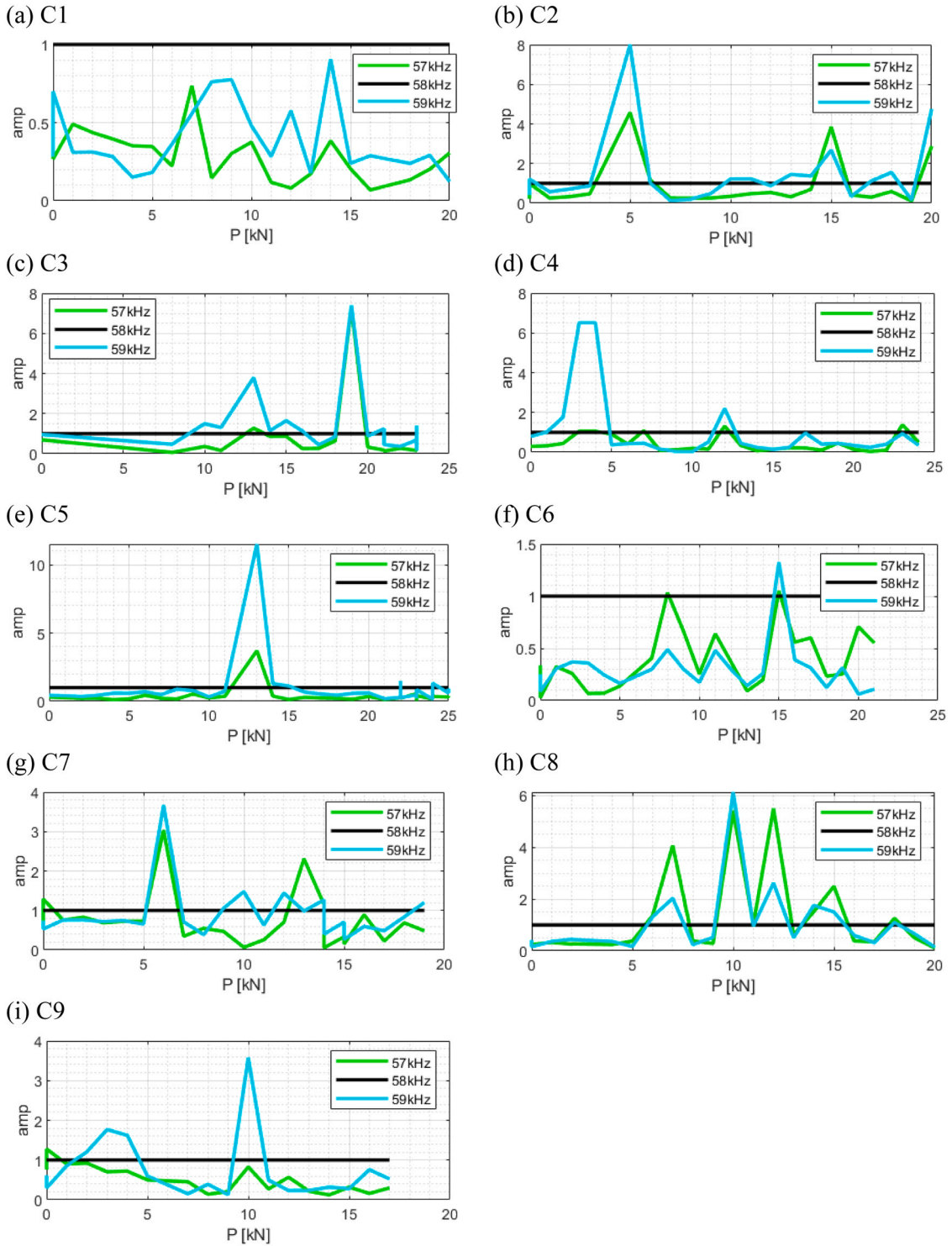(f) C6

(g) C7

(h) C8

(i) C9

**Fig. 16.** Spectra of ultrasonic signals measured for specimen C1-C9.

(Fig. 19). For each velocity map, a mean value, standard deviation (STD), and coefficient of variation (COV) were calculated. Additionally, absolute and relative changes in mean velocity, STD, and COV were determined and the examples are presented in Fig. 20.

It can be seen that the maps for the first measurement are rather smooth and do not have any significant perturbations. On the contrary, the maps for the second measurement (after corrosion) show some points with a lower value of wave velocity, mostly for

Table 5
The values of the load for which the phenomenon was observed.

Specimen	C1	C2	C3	C4	C5	C6	C7	C8	C9
Type of failure mode	A	A	A	A	A	B	B	B	B
The value of the load [kN]	-	5 and 15	13 and 19	4 and 12	13	15	6	7–14, max at 10	10
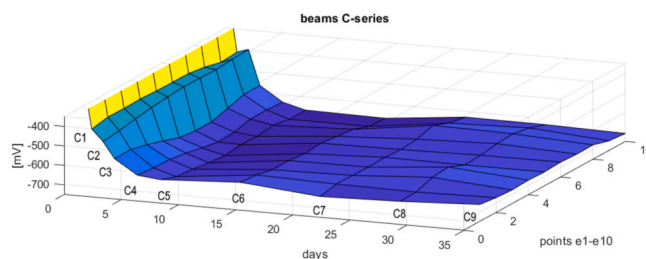
Fig. 17. The potential measured on beams.

Table 6
The mean values of measured potential in each specimen.

Specimen	C1	C2	C3	C4	C5	C6	C7	C8	C9
Measured potential [mV] (vs Cu|CuSO$_4$)	−450	−474	−640	−700	−726	−696	−680	−670	−680

Table 7
The values of the first, the second, and the third natural frequencies before and after immersion.

specimen		C1	C2	C3	C4	C5	C6	C7	C8	C9
f1 [Hz]	before immersion	496	518	513	519	504	517	522	535	514
	after immersion	533	540	537	544	538	555	558	567	543
	increase	107.5	104.4	104.6	104.9	106.7	107.4	107	105.9	105.7
f2 [Hz]	before immersion	1237	1286	1275	1281	1248	1275	1301	1315	1274
	after immersion	1319	1341	1338	1346	1331	1360	1384	1386	1343
	increase	106.6	104.3	104.9	105.1	106.7	106.7	106.4	105.4	105.4
f3 [Hz]	before immersion	2155	2258	2239	2235	2200	2227	2272	2293	2236
	after immersion	2288	2337	2343	2352	2334	2355	2405	2385	2318
	increase	106.2	103.5	104.6	105.2	106.1	105.7	105.9	104	103.6

beams with the longest duration of corrosion. The location of these points corresponds to the image of cracks (lower velocity values are the effect of the elongation of the propagation paths).

While observing the graphs representing the evolution of the values over the time of corrosion, it can be seen that the beams gave slightly different initial values of the wave velocity (from the first measurement, before corroding) varying between 3940 m/s and 4100 m/s. The values of COV were between 3.9 % and 5.4 %, thus the material was considered homogeneous. After corrosion, the values of mean velocity increased for all beams because the samples were soaked with water that allowed the P-wave to travel with higher velocity. In this case, mean velocity was considered to be a poor indicator of damage. On the other hand, it can be seen that the corresponding STD and COV increased significantly with the corrosion time between approximately 3.5 % (shortest corrosion time) and almost 9 % (longest corrosion time). Importantly, this change was almost linear (the correlation coefficient was 0.9845). The increase in COV resulted from the presence of points with lower velocity values as a consequence of crack formation.

5. Conclusions

The paper deals with both non-destructive and destructive tests conducted on steel-reinforced concrete beams subjected to accelerated electrochemical corrosion. A total number of ten specimens were examined, using both non-destructive and destructive methods to investigate the occurrence of corrosion.

Accelerated electrochemical corrosion was induced by keeping the specimens in a 3.5 % NaCl solution for the predetermined number of days – from 1 to 35 and by generating constant current flowing through the specimen at a value of 90 mA. Each specimen was tested before and after being exposed to corrosion. Based on the observations and the results obtained, the following conclusions can be formulated:
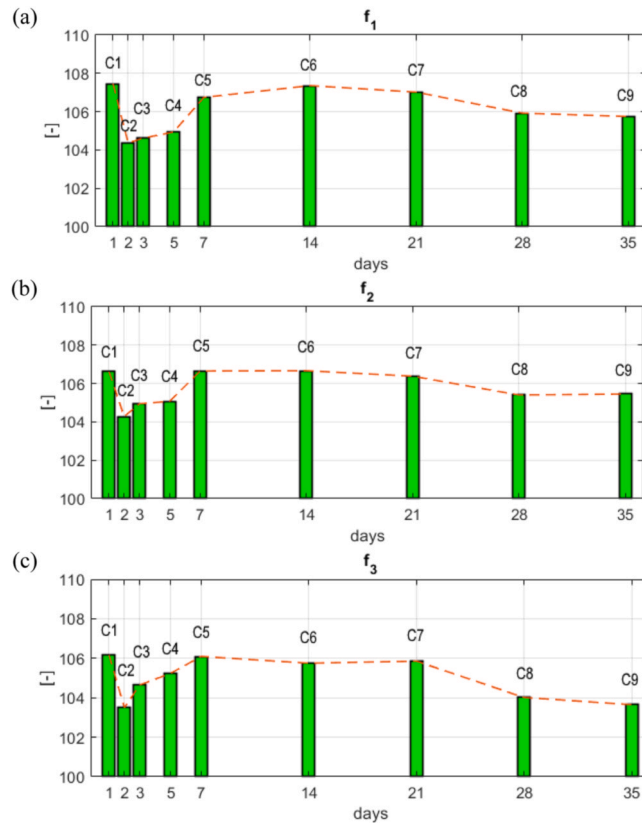
Fig. 18. Relative differences between measurements of natural frequencies of free vibrations: (a) f_1, (b) f_2, (c) f_3.

- After visual inspection after specimen immersion, cracks caused by corrosion were observed in specimens C3-C9, which were immersed in the solution for 3–35 days. No cracks occurred in specimens C1 and C2.
- Two failure modes were observed in a three-point bending test, i.e., "type A" (flexural failure) and "type B" (shear failure). For specimens that were kept in the solution for a shorter time, type A was dominant, in which damage to the specimens was caused by the stress level that was equal to the yield point of the rebar. However, for the specimens that were kept in the solution longer, a different scheme was observed (type B), in which the diagonal and longitudinal cracks occurred as a result of the loss of adhesion of the bar to the concrete and, then, detachment. The lowest capacity was obtained for specimen C9, which was immersed in the NaCl solution for the longest time.
- Modulated ultrasonic wave tests allowed to determine the spectra consisting of a dominant component with a frequency of 58 kHz and one component with a frequency of 57 kHz and 59 kHz. Generally, the amplitudes of the sideband components were smaller than the amplitude of the carrier wave. However, for a specific value of force applied during a three-point bending the amplitude values that occurred in the sidebands were higher than the amplitude of the carrier wave.
- For all specimens, the potential difference between the reinforced steel bar and a reference electrode placed on their bottom surface increased. The values of the measured potential difference varied from about -440 mV for specimens that were immersed in NaCl solution for the shortest time (C1 and C2), to about -740 mV (both vs Cu|CuSO$_4$). The values of the measured potential decreased the most in specimen C3 compared to C2, being about 35 %. Such a significant difference in potential may be caused by the appearance of the first cracks in specimen C3.
- The values of the first, the second, and the third natural frequencies increased for all specimens. The highest increase in frequencies was obtained for specimen C1. Moreover, the increase of the first frequency remained at the same level for all specimens, while the increase of the second and the third frequencies decreased with the time that specimens were immersed in the solution.
- The maps of the measured velocity of the P-wave passing through the specimens before and after immersion showed some points with a lower value of the wave velocity. The location of these points corresponded to the image of cracks (lower velocity values were the effect of the elongation of propagation paths). All measured P-wave velocities increased after immersion of the specimens.

The methodology presented in this paper for diagnosing the occurrence of corrosion in reinforced concrete beams has shown that corrosion can be successfully detected by non-destructive methods before it is visually apparent on the external surface of the specimen. However, a destructive method can also be successfully developed and supplemented.
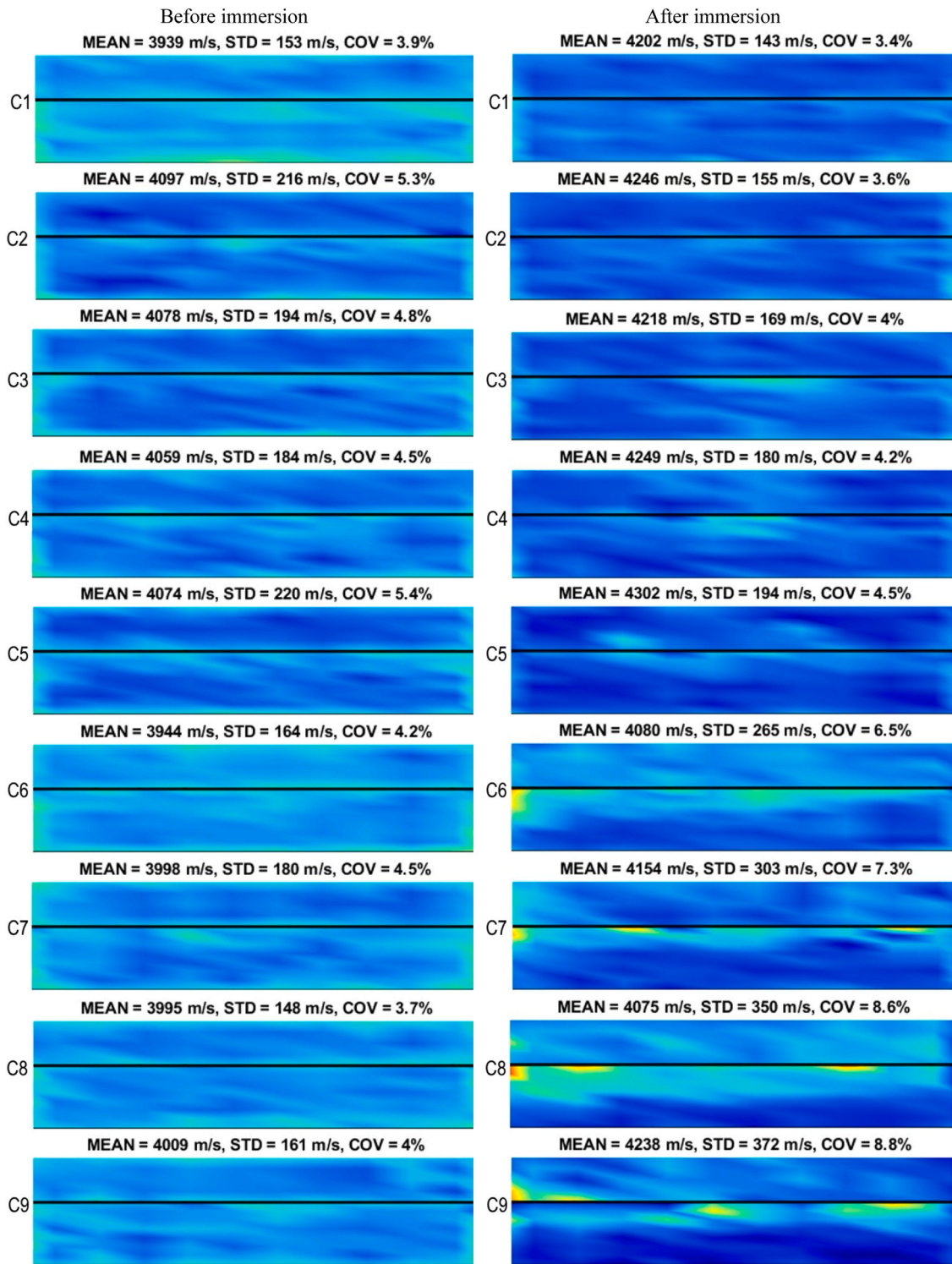
Fig. 19. The values of P-wave velocities before (on the left) and after (on the right) immersion.
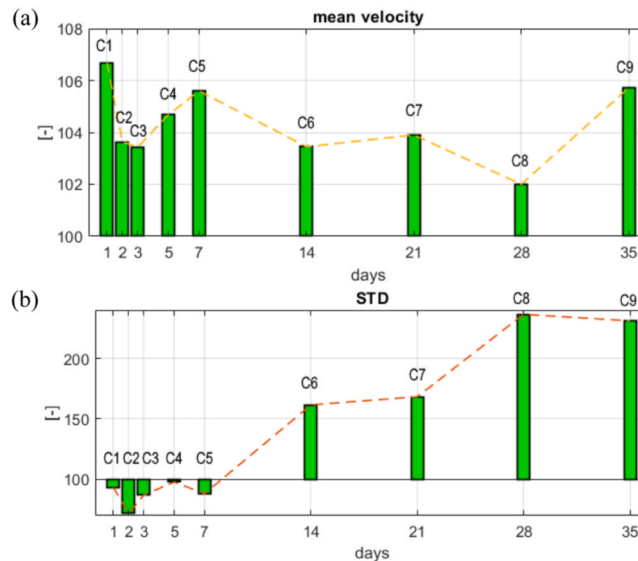
CRediT authorship contribution statement

Fig. 20. Relative differences between measurements: (a) mean velocities, (b) STD.

Writing – review & editing, Supervision, Methodology, Conceptualization. **Blazej Meronk:** Software, Methodology, Investigation, Data curation.

Declaration of Competing Interest

The authors declare that they have no known competing financial interests or personal relationships that could have appeared to influence the work reported in this paper.

Data Availability

Data will be made available on request.

Acknowledgments

References

[1] P.K. Mehta, P.J. Monteiro, Microstructure and properties of hardened concrete, Concr.: Microstruct. Prop. Mater. (2006) 41–80.
[2] Guoyi Zhang Ye Tian, Qiang Zeng Hailong Ye, Zushi Tian Zhidong Zhang, Nanguo Jin Xianyu Jin, Jiaxi Wang Zhonggou Chen, Corrosion of steel rebar in concrete induced by chloride ions under natural environments, Constr. Build. Mater. 369 (2023) 130504, https://doi.org/10.1016/j.conbuildmat.2023.130504.
[3] Xiaoning Cui, Qicai Wang, Sheng Li, Jinpeng Dai, Chao Xie, Yun Duan, Jianqiang Wang, Deep learning for intelligent identification of concrete wind-erosion damage, Autom. Constr. 141 (2022) 104427, https://doi.org/10.1016/j.autcon.2022.104427.
[4] Zhi Zheng, Chunyang Su, Xiaolan Pan, Ye Sun, Wei Yuan, Wentao Wang, Quantitative damage evaluation of prestressed concrete containments with steel fiber strengthening under internal pressure, Eng. Struct. 278 (2023) 115494, https://doi.org/10.1016/j.engstruct.2022.115494.
[5] Li. Zhu Xin-Lin Ji, Guang-Ming Wang Ray Kai-Leung Su, Lateral overturning process and failure mechanism of curved steel-concrete composite box-girder bridges under specific overloading vehicles, Structures 35 (2022), https://doi.org/10.1016/j.istruc.2021.11.039.
[6] Cheng Hu, Xingzhong Weng, Jun Zhang, Wei Xu, Bo Qu, Lihai Su, Experimental study on fatigue strength of airport concrete pavement slab, Constr. Build. Mater. 270 (2021) 121493, https://doi.org/10.1016/j.conbuildmat.2020.121493.
[7] L. Mazzon, G. Frappa, M. Pauletta, Effectiveness of tuned mass damper in reducing damage caused by strong earthquake in a medium-rise building (art. no), Appl. Sci. (Switz.) 13 (11) (2023) 6815, https://doi.org/10.3390/app13116815.
[8] Frappa, G.; Pauletta, M. Seismic retrofitting of a reinforced concrete building with strongly different stiffness in the main directions. In Proceedings of 14th fib International PhD Symposium in Civil Engineering, Rome, Italy, 5-7 September 2022.
[9] Chuanqing Fu, Nanguo Jin, Hailong Ye, Xianyu Jin, Wei Dai, Corrosion characteristics of a 4-year naturally corroded reinforced concrete beam with load-induced transverse cracks, Corros. Sci. 117 (2017), https://doi.org/10.1016/j.corsci.2017.01.002.
[10] Xingji Zhu, Goangseup Zi, A 2D mechano-chemical model for the simulation of reinforcement corrosion and concrete damage, Constr. Build. Mater. 137 (2017), https://doi.org/10.1016/j.conbuildmat.2017.01.103.
[11] Eliass El Alami, Fatima-Ezzahra Fekak, Luigi Garibaldi, Ahmed Elkhalfi, A numerical study of pitting corrosion in reinforced concrete structures, J. Build. Eng. 43 (2021) 102789, https://doi.org/10.1016/j.jobe.2021.102789.
[12] Francesco Freddi, Lorenzo Mingazzi, A predictive phase-field approach for cover cracking in corroded concrete elements, Theor. Appl. Fract. Mech. 122 (2022) 103657, https://doi.org/10.1016/j.tafmec.2022.103657.

[13] Xianyu Jin, Jing Tong, Ye Tian, Nanguo Jin, Time-varying relative displacement field on the surface of concrete cover caused by reinforcement corrosion based on DIC measurement, Constr. Build. Mater. 159 (2018), https://doi.org/10.1016/j.conbuildmat.2017.10.119.

[14] Raja Rizwan Hussain, Abdulrahman M. Alhozaimy, Abdulaziz Al-Negheimish, Effect of curing compounds on the quality of passive layer development under varying oxygen concentration for RC structures in the course of early curing of concrete, Constr. Build. Mater. 350 (2022) 128842, https://doi.org/10.1016/j.conbuildmat.2022.128842.

[15] Romain Rodrigues, Stéphane Gaboreau, Julien Gance, Ioannis Ignatiadis, Stéphanie Betelu, Reinforced concrete structures: A review of corrosion mechanisms and advances in electrical methods for corrosion monitoring, Constr. Build. Mater. 269 (2021) 121240, https://doi.org/10.1016/j.conbuildmat.2020.121240.

[16] Nabil Al-Akhras, Rawan Aleghnimat, Evaluating corrosion deterioration in self-compacted reinforced concrete beams and prisms using different tests, Constr. Build. Mater. 256 (2020) (2020) 119347, https://doi.org/10.1016/j.conbuildmat.2020.119347.

[17] Jinwei Chen, Chuanqing Fu, Hailong Ye, Xianyu Jin, Corrosion of steel embedded in mortar and concrete under different electrolytic accelerated corrosion methods, Constr. Build. Mater. 241 (2020) (2020) 117971, https://doi.org/10.1016/j.conbuildmat.2019.117971.

[18] M. Dai, O. Yang, Y. Xiao, et al., Influence of longitudinal bar corrosion on impact behavior of RC beams, Mater. Struct. 49 (2016) 3579–3589, https://doi.org/10.1617/s11527-015-0741-0.

[19] M. Maalej, C.Y. Chhoa, S.T. Quek, Effect of cracking, corrosion and repair on the frequency response of RC beams, Constr. Build. Mater. 24 (2010) 719–731, https://doi.org/10.1016/j.conbuildmat.2009.10.036.

[20] Benjamin L. Ervin, Daniel A. Kuchma, Jennifer T. Bernhard, Henrique Reis, Monitoring corrosion of rebar embedded in mortar using high-frequency guided ultrasonic waves (January 2009), J. Eng. Mech. 135 (1) (2009), https://doi.org/10.1061/(ASCE)0733-9399(2009)135:1(9).

[21] C. Lejouad, B. Richard, P. Mongabure, S. Capdevielle, F. Ragueneau, et al. Effect of steel reinforcement corrosion on the dynamic behavior of RC beams. FONTEVRAUD9 - International Symposium: Contribution of Materials Investigations and Operating Experience to Light Water NPPs' Safety, Performance and Reliability, Sep2018, Avignon, France. cea-02338541.

[22] F. Tondolo, Bond behaviour with reinforcement corrosion, Constr. Build. Mater. 93 (2015), https://doi.org/10.1016/j.conbuildmat.2015.05.067.

[23] D. Luo, Y. Li, J. Li, K.-S. Lim, N.A.M. Nazal, H. Ahmad, A recent progress of steel bar corrosion diagnostic techniques in RC structures, Sensors 19 (2019) 34, https://doi.org/10.3390/s19010034.

[24] Sanjeev Kumar Verma, Sudhir Singh Bhadauria, Saleem Akhtar, Monitoring corrosion of steel bars in reinforced concrete structures, Sci. World J. 2014 (2014) 957904, https://doi.org/10.1155/2014/957904.

[25] J.Y. Hu, S.S. Zhang, E. Chen, W.G. Li, A review on corrosion detection and protection of existing reinforced concrete (RC) structures, Constr. Build. Mater. 325 (2022) 126718, https://doi.org/10.1016/j.conbuildmat.2022.126718.

[26] M. Pour-Ghaz, O.B. Isgor, P. Ghods, Quantitative interpretation of half-cell potential measurements in concrete structures, J. Mater. Civ. Eng. 21 (Issue 9) (2009), https://doi.org/10.1061/(ASCE)0899-1561(2009)21:9(467).

[27] Liye Zhang, Limin Sun, Lijuan Dong, Experimental study on the relationship between the natural frequency and the corrosion in reinforced concrete beams (Article ID), Adv. Mater. Sci. Eng. 2021 (2021) 9976738, https://doi.org/10.1155/2021/9976738.

[28] Ashutosh Sharma, Shruti Sharma, Sandeep Sharma, Abhijit Mukherjee, Ultrasonic guided waves for monitoring corrosion of FRP wrapped concrete structures, Constr. Build. Mater. 96 (2015), https://doi.org/10.1016/j.conbuildmat.2015.08.084.

[29] Yuqing Liu, Weijian Ding, Peng Zhao, Lei Qin, Tomoki Shiotani, Research on in-situ corrosion process monitoring and evaluation of reinforced concrete via ultrasonic guided waves, Constr. Build. Mater. 321 (2022) 126317, https://doi.org/10.1016/j.conbuildmat.2022.126317.

[30] Jianjun Han, Zhuang Miao, Julian Wang, Xianlei Zhang, Yajun Lv, Investigation of the corrosion-induced damage mechanism of steel fibers in ultra-high-performance steel fiber-reinforced concrete using X-ray computed tomography, Constr. Build. Mater. 368 (2023) 130429, https://doi.org/10.1016/j.conbuildmat.2023.130429.

[31] Fabien Bernachy-Barbe, Takwa Sayari, V.éronique Dewynter-Marty, Valérie L'Hostis, Using X-ray microtomography to study the initiation of chloride-induced reinforcement corrosion in cracked concrete, Constr. Build. Mater. 259 (2020) 119574, https://doi.org/10.1016/j.conbuildmat.2020.119574.

[32] Samanta Robuschi, Alessandro Tengattini, Jelke Dijkstra, Ignasi Fernandez, Karin Lundgren, A closer look at corrosion of steel reinforcement bars in concrete using 3D neutron and X-ray computed tomography, Cem. Concr. Res. 144 (2021) 106439, https://doi.org/10.1016/j.cemconres.2021.106439.

[33] Priya Goyal, Shruti Sharma, Naveen Kwatra, Acoustic emission monitoring of steel fiber reinforced beams under simultaneous corrosion and sustained loading, Eur. J. Environ. Civ. Eng. (2022), https://doi.org/10.1080/19648189.2022.2087743.

[34] Reza Goldaran, Ahmet Turer, Mehdi Kouhdaragh, Kezban Ozlutas, Identification of corrosion in a prestressed concrete pipe utilizing acoustic emission technique, Constr. Build. Mater. 242 (2020) 118053, https://doi.org/10.1016/j.conbuildmat.2020.118053.

[35] Bai Yanjie, Su Hui, Yin Bai, Yuebo Cai, Mechanical properties and damage mechanisms of concrete under four temperature gradients combined with acoustic emission method, J. Build. Eng. 57 (2022) 104906, https://doi.org/10.1016/j.jobe.2022.104906.